Journal of Biomedical Optics 5(2), 237–247 (April 2000)

Three-dimensional diffuse optical mammography with ultrasound localization in a human subject

M. J. Holboke
University of Pennsylvania
Department of Physics and Astronomy
Philadelphia, Pennsylvania 19104

B. J. Tromberg
University of California Irvine
Beckman Laser Institute
Irvine, California 92612

X. Li
Massachusetts Institute of Technology
Department of Electrical Engineering
Boston, Massachusetts

N. Shah
J. Fishkin
University of California Irvine
Beckman Laser Institute
Irvine, California 92612

D. Kidney
University of California Irvine Medical Center
Department of Radiology
Irvine, California 92612

J. Butler
University of California Irvine Medical Center
Department of Surgery
Irvine, California 92612

B. Chance
University of Pennsylvania
Department of Biochemistry and Biophysics
Philadelphia, Pennsylvania 19104

A. G. Yodh
University of Pennsylvania
Department of Physics and Astronomy
Philadelphia, Pennsylvania 19104

Abstract. We describe an approach that combines clinical ultrasound and photon migration techniques to enhance the sensitivity and information content of diffuse optical tomography. Measurements were performed on a postmenopausal woman with a single 1.8×0.9 cm malignant ductal carcinoma *in situ* approximately 7.4 mm beneath the skin surface (UCI IRB protocol 95-563). The ultrasound-derived information about tumor geometry enabled us to segment the breast tissue into tumor and background regions. Optical data was obtained with a multifrequency, multiwavelength hand-held frequency-domain photon migration backscattering probe. The optical properties of the tumor and background were then computed using the ultrasound-derived geometrical constraints. An iterative perturbative approach, using parallel processing, provided quantitative information about scattering and absorption simultaneously with the ability to incorporate and resolve complex boundary conditions and geometries. A three to four fold *increase* in the tumor absorption coefficient and nearly 50% reduction in scattering coefficient relative to background was observed ($\lambda=674$, 782, 803, and 849 nm). Calculations of the mean physiological parameters reveal fourfold greater tumor total hemoglobin concentration $[\mathrm{Hb_{tot}}]$ than normal breast (67 μM vs 16 μM) and tumor hemoglobin oxygen saturation (SOx) values of 63% (vs 73% and 68% in the region surrounding the tumor and the opposite normal tissue, respectively). Comparison of semi-infinite to heterogeneous models shows superior tumor/background contrast for the latter in both absorption and scattering. Sensitivity studies assessing the impact of tumor size and refractive index assumptions, as well as scan direction, demonstrate modest effects on recovered properties. *© 2000 Society of Photo-Optical Instrumentation Engineers.* [S1083-3668(00)01502-1]

Keywords: diffuse optical tomography; near infrared imaging; photon migration; breast optical properties

Paper JBO-024 received Oct. 30, 1999; revised manuscript received April 10, 2000; accepted for publication April 10, 2000.

1 Introduction

The unique functional information and deep tissue penetration provided by near-infrared (NIR) light makes it well suited for characterizing and imaging breast tumors. However, optical contrast elements associated with malignant and benign lesions as well as normal breast tissue physiological fluctuations are poorly understood. Consequently, NIR transillumination techniques that do not separate light absorption from scattering may not provide sufficient diagnostic information to be clinically useful. In order to address this issue, time- and frequency-domain photon migration (PM) techniques have been developed to facilitate quantitative tissue analysis and separation of tissue absorption and scattering properties *in vivo*. When multiwavelength time- or frequency-domain photon migration (FDPM) are combined with tomographic techniques, such as diffuse optical tomography (DOT), then it is possible to construct low-resolution (0.5–1 cm) functional images of intrinsic tissue physiology; e.g., tissue hemoglobin (total, oxy-, and deoxyforms), oxygen saturation, blood volume fraction, water content, fat content, and cellular structure.

In order to perform DOT, measurements of remitted diffuse light intensity and time-of-flight (or photon density wave phase and amplitude) are made on the boundary of the tissue, and are then used to reconstruct the absorption and scattering optical properties of the underlying medium. A variety of methods have been developed for DOT. These include fits to analytic solutions,[1–3] backprojection methods,[4–7] diffraction tomography in *k*-space,[8–14] perturbation approaches,[15–30] elliptic systems method (ESM),[31–33] and a direct method.[34] All of these approaches have various advantages and disadvantages. Simple boundary conditions and geometries reduce computational cost and increase speed, but also reduce quantitative information about the system. On the

---

Address all correspondence to B. J. Tromberg. Tel: 949-824-8705; Fax: 949-824-6969; E-mail: tromberg@bli.uci.edu and A. G. Yodh, Tel: 215-898-6345, E-mail: yodh@dept.physics.upenn.edu

1083-3668/2000/$15.00 © 2000 SPIE

other hand, DOT reconstructions are sensitive to many parameters including complex internal geometry of tissues, and at a high computational cost provide access to this information. In this article we employ an iterative perturbative approach that yields quantitative information about scattering and absorption simultaneously, and has the ability to resolve complex boundary conditions and geometries. However, the method is slow and computationally expensive, especially in three-dimensions (3D). Therefore, we have implemented the algorithm using parallel processing to reduce the computational processing time.

Our reconstruction is enhanced by the use of clinical ultrasound measurements to locate the tumor and assess its size. Using this information about tumor geometry, we segment the breast into two regions: tumor and background. Our data is derived at multiple frequencies using a simple, hand-held backscattering probe that contains relatively few source-detector separations.[35] This scheme of combining ultrasound and optical information has been suggested as a means to improve breast tumor diagnostics and an instrument employing these modalities simultaneously has been demonstrated in phantoms.[36] To our knowledge, this work represents the first *in vivo* investigation along these lines.

The optical properties of the tumor and background are computed based on the data and the geometrical constraints. We compare our results to analytic models in order to demonstrate the utility of image segmentation for quantitative tumor spectroscopy. Factors that influence the recovered properties, such as tumor size, refractive index, and scan direction are examined. Finally, the resultant optical properties are used to calculate tumor and normal tissue hemoglobin content and hemoglobin oxygen saturation in order to gain insight into the relationship between optical and physiological changes associated with malignant tumor growth.

2 Methods

2.1 FDPM Instrument

FDPM instrumentation and theoretical background have been described in detail.[35] Briefly, the core component of the FDPM apparatus is a network analyzer (Hewlett Packard, model 8753C), which is used to produce modulation swept from 300 kHz to 1 GHz [20 dBm radio-frequency (rf) output]. rf from the network analyzer is serially superimposed [via the alternating-current (ac) switch] on the direct current of up to eight different diode lasers (e.g., 674, 782, 803, 849, 894, and 956 nm) using individual bias tees (model 5575 A, Picosecond Pulse Labs) and an rf switch (model 8768 K, Hewlett Packard). 100-μm-diam gradient-index fibers are used to couple each light source to an 8×8 optical multiplexer (model GP700, DiCon Instruments). The 8×8 optical multiplexer allows for up to eight different diode laser light sources and eight different optical fiber positions.

Light is launched onto the tissue (or test object) using the above-mentioned unique wavelengths and one source fiber. An avalanche photodiode [(APD), Hamamatsu, model C5658] is used to detect the diffuse optical signal that propagates through the biological tissue. Both the APD and probe end of the source optical fiber are fabricated into a hand-held probe. The probe is in direct contact with the patient and can be scanned over the surface. The optical power coupled into the tissue averages approximately 10–30 mW. Measurement time depends on the precision required, the number of sweeps performed, and rf optical switch times. For human subject studies, approximately 0.1 s is used to sweep over the entire 1 GHz band of modulation frequencies. However, total elapsed time for four diodes (typically 12–16 sweeps/diode), data transfer, display, and source switching is approximately 40 s. Most components, including the network analyzer, rf optical switches, diode power supplies, and temperature of diode mounts are controlled by computer using virtual instrument software (LabView, National Instruments).

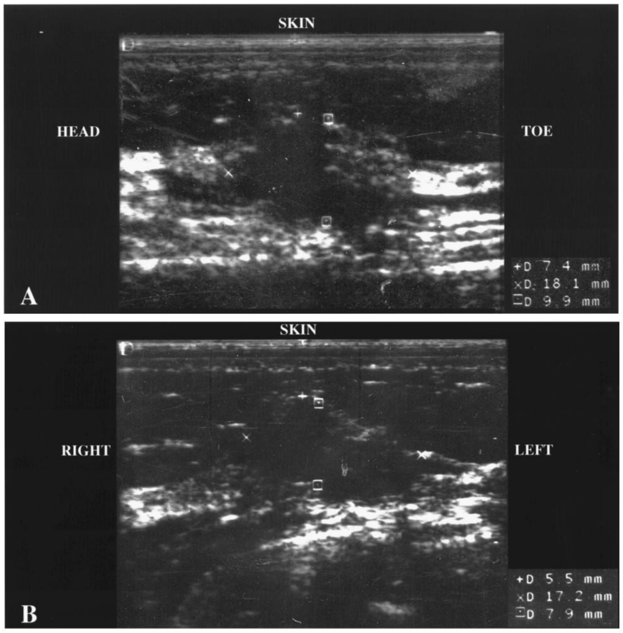

Fig. 1 (A) saggital and (B) axial ultrasound images of breast tumor.

2.2 Measurements

Experiments were performed under the guidelines of UC Irvine IRB-approved protocol No. 95-563. The patient was a 67 year old postmenopausal woman with a single palpable mass approximately 7.4 mm beneath the skin surface in the upper outer quadrant of the left breast. Histological examination following surgical biopsy and prebiopsy ultrasound revealed a roughly 1.8×0.9 cm ductal carcinoma *in situ* (DCIS) (malignant tumor). Ultrasound images along the sagittal and axial planes supplied geometry and location information about the tumor (see Figure 1). The location, dimension, and depth of the tumor are reported in Table 1.

Table 1 Elliptical tumor geometry: *a* is along the *y* axis (sagittal), *b* is along the *x* axis (axial), *c* is along the *z* axis, *zc* is the depth of the center of the tumor below the skin surface. Relative positioning of the tumor to the source-detector pairs can be seen in Figure 1.

Plane	*a*	*b*	*c*	*zc*
Sagittal	2.13 cm		1.17 cm	1.325 cm
Axial		1.68 cm	1.09 cm	1.065 cm

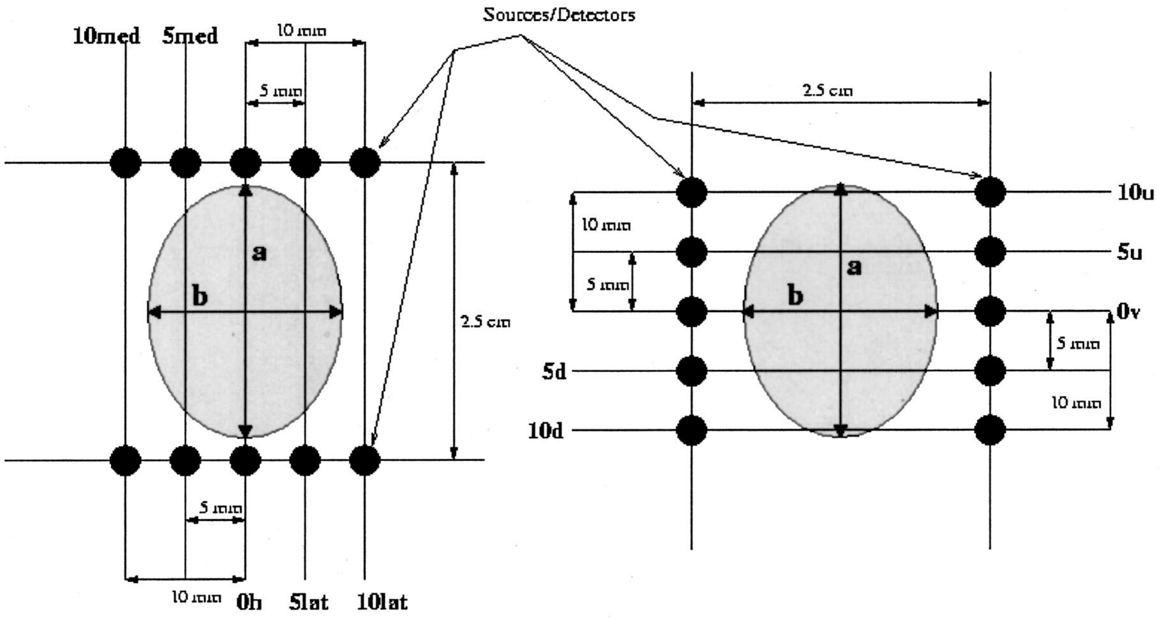

Fig. 2 Source-detector pair locations along the sagittal (left, the horizontal measurements) and axial (right, the vertical measurements) planes centered with respect to the tumor. The 0*h* position is the source-detector pair centered over the tumor for the horizontal measurements, 0*v* is similar but for the vertical measurements. Med refers to medial, i.e., towards the middle of the body, and lat refers to lateral, i.e., towards the side of the body. *u* refers to up, which is towards the head and *d* refers to down, i.e., towards the feet. The tumor geometrical constants *a* and *b* are listed in Table 1.

This information was then used to center the optical measurement pad over the tumor. Here we have assumed that the ultrasound-defined margins are the same as the optical margins. This assumption could be incorrect, if alterations due to neovascular density and tissue inflammatory response occur beyond the ultrasound-defined tumor region and are detected optically, but not ultrasonically.

Optical measurements were performed by placing the FDPM probe on both a normal and a tumor-containing breast. Data were acquired using the hand-held scanning probe placed in 10 discrete locations covering a 2×2 cm grid mapped onto the breast surface (Figure 2). The probe source-detector (s-d) pair was fixed at 2.5 cm in separation and the probe was placed on the tissue with the source and detector bracketing the tumor. Photon migration data were acquired by moving the probe in 0.5 cm increments along inferior-superior and medial-lateral paths. Repeat measurements immediately above tumor center were obtained at least 3 times. Both normal and tumor-containing breasts were studied.

Sequential scans of the same location following probe removal and replacement revealed no significant variation ($<5\%$) in optical properties. Normal tissue measurements were acquired in the same manner from a symmetric site on the opposite, uninvolved breast (Figure 3). Phase and amplitude data (represented by $\Box$ and A, respectively) obtained from tumor measurements are shown in Figure 4. We only utilized frequencies below 400 MHz due to high frequency noise. Additionally, the wavelengths 894 and 956 nm suffered from modulation artifacts and were not employed.

2.3 Diffuse Optical Mammography Segmentation and Analytic Schemes

The segmentation and semi-infinite analytic fits are accomplished using diffusion theory in the frequency domain to describe the propagation of light in breast tissue.[37] The equation is

$$\nabla\cdot(D(\mathbf{r})\nabla\Phi(\mathbf{r},\omega))+\left(\frac{i\omega}{c}-\mu_a(\mathbf{r})\right)\Phi(\mathbf{r},\omega)=-S(\mathbf{r},\omega), \tag{1}$$

with the following boundary condition:

$$\frac{\partial\Phi}{\partial\hat{n}}=-\alpha\Phi. \tag{2}$$

$D(\mathbf{r})$ is the diffusion coefficient and is equivalent to $1/3\mu_s(\mathbf{r})'$. $\mu_s'(\mathbf{r})$ and $\mu_a(\mathbf{r})$ are the scattering and absorption coefficients respectively. $\Phi(\mathbf{r},\omega)$ is the diffuse photon density, ω is the frequency modulation, and c is the speed of light in the media. $S(\mathbf{r},\omega)$ is the source term, approximated as a delta function $1/\mu_s'$ in from the boundary. α is equal to $[(1-R_{\mathrm{eff}})/(1+R_{\mathrm{eff}})](3\mu_s'/2)$, where R_{eff} is approximated by $-1.440n^{-2}+0.170n^{-1}+0.668+0.063n$,[38] and n is equal to $n_{\mathrm{in}}/n_{\mathrm{out}}$, the index of refraction mismatch at the tissue/air interface boundary.

All iterative perturbative approaches follow a similar algorithm. First, the optical properties are estimated. Second, the forward problem [Eq. (1)] is solved. Third, a χ^2 (i.e., $\chi^2=\Sigma_{i=1}^{NM}(\Phi_i^m-\Phi_i^c)^2$, where NM is the number of measure-

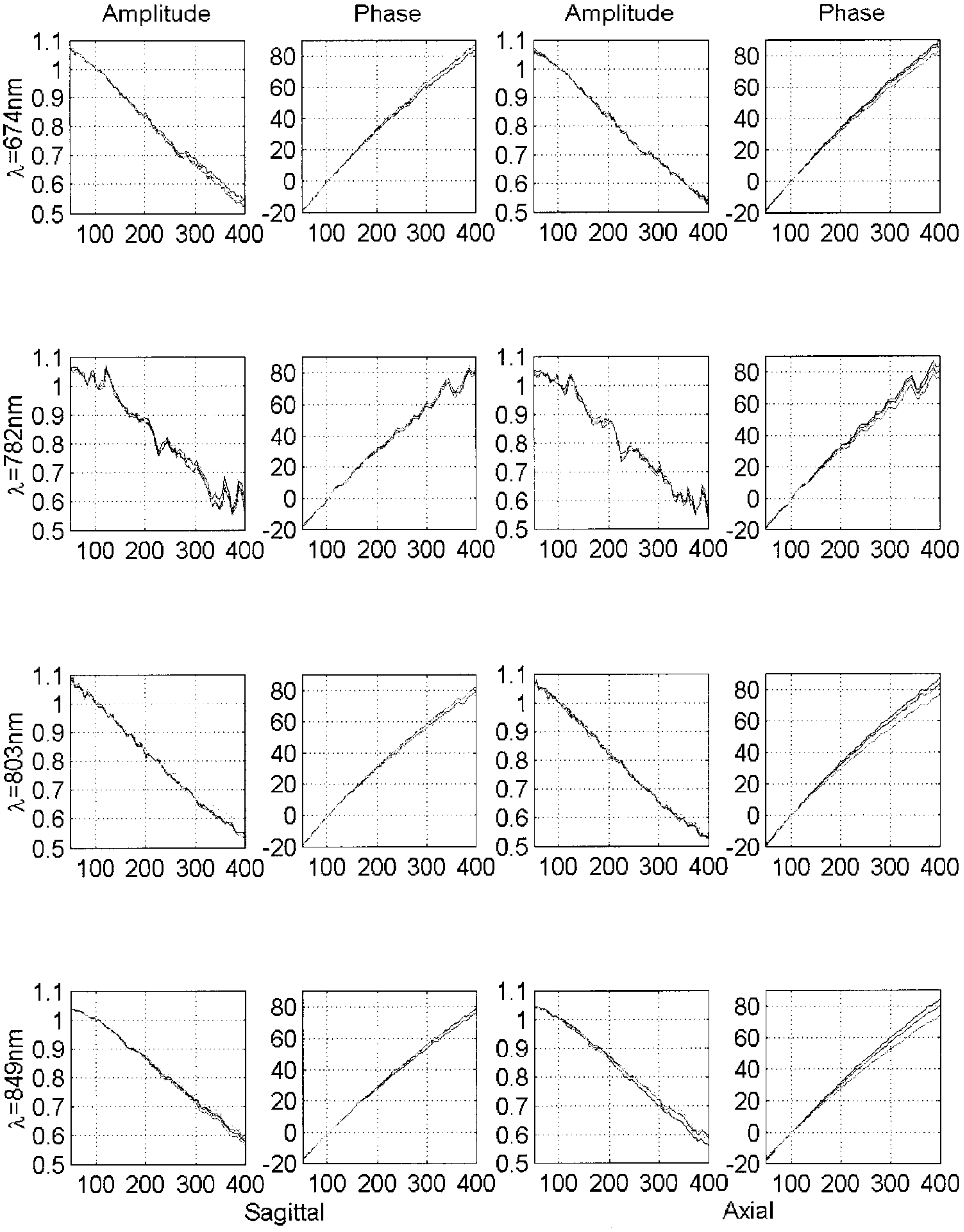

Fig. 3 Measurements for each optical wavelength over the entire modulation frequency range for the normal breast. Source-detector pairs along sagittal planes (left, horizontal measurements) have blue for 10 med, green for 5 med, red for 0*h*, cyan for 5 lat, and magenta for 10 lat; along axial planes (right) vertical measurements have blue for 10*d*, green for 5*d*, red for 0*v*, cyan for 5*u*, and magenta for 10*u*. See Figure 1, for detector positioning. Measurements over 400 MHz suffer from systematic noise and the 894 and 956 nm wavelengths have significant artifacts below 400 MHz also. These measurements, therefore, are not used in the semi-infinite analytic fits.

ments, Φ^m is the measured data, and Φ^c is the numerically calculated data) is calculated and convergence is checked. Fourth, the inverse problem is setup (i.e., the Jacobian is determined). Fifth, the optical property perturbations are solved for (i.e., the inverse problem is solved). Finally, the optical properties are updated and a return to the second step occurs. Within these approaches there are a couple of methods to solving the forward problem and for determining the Jacobian [for a review see Ref. 39]. Additionally, there have been a variety of methods developed for solving the inverse problem.[40–48] We have chosen to follow a Green's function (or adjoint) method.[15–18,27,28] The inverse problem, therefore, is formulated in the following way:

$$\begin{aligned}&\int \Phi(\mathbf{r},\omega)G(\mathbf{r},\omega)\Delta\mu_a(\mathbf{r})d\nu\\&\quad+\int \nabla\Phi(\mathbf{r},\omega)\cdot\nabla G(\mathbf{r},\omega)\Delta D(\mathbf{r})d\nu\\&\quad=-(\Phi^m(\mathbf{r}_d,\omega)-\Phi^c(\mathbf{r}_d,\omega))\end{aligned}\qquad(3)$$

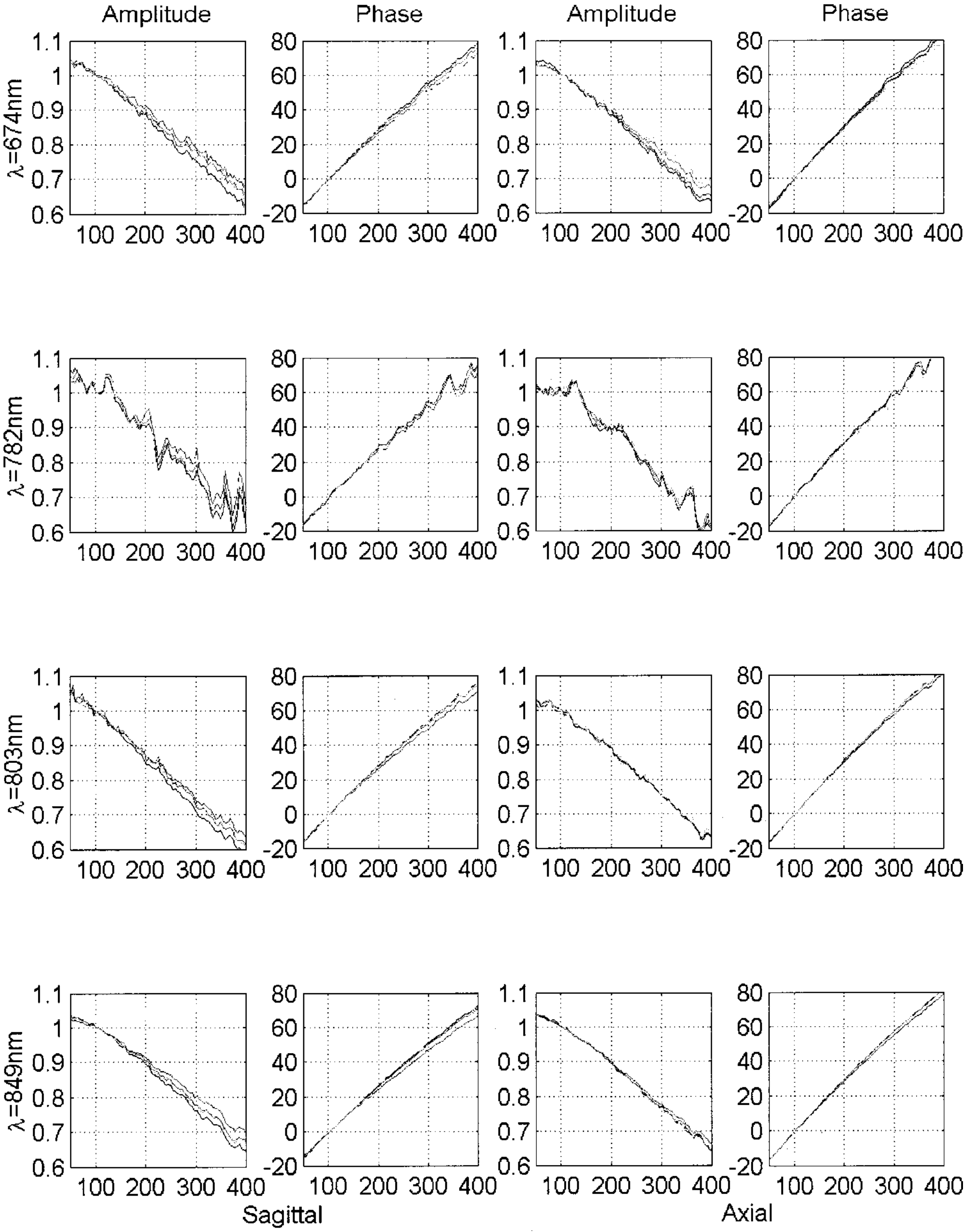

Fig. 4 Similar to Figure 3, but for the breast with lesion. Measurements over 400 MHz suffer from systematic noise and the 894 and 956 nm wavelengths have significant artifacts below 400 MHz as well. Similar to the normal breast these measurements are not used in the semi-infinite analytic fits nor are they used in the segmented reconstruction.

or in matrix form:

$$[\mathbf{J}]\{\Delta\mu_a(\mathbf{r}),\Delta D(\mathbf{r})\}^T=-\{\Phi^s(\mathbf{r}_d,\omega)\}, \tag{4}$$

where $\mathbf{r}_d$ is the position of the detectors, Φ^m refers to the measurements, Φ^c are the calculated values, $\Phi^s=\Phi^m-\Phi^c$, and $\mathbf{J}$ is the Jacobian. The Green's function satisfies the following adjoint problem:

$$\nabla\cdot(D(\mathbf{r})\nabla G(\mathbf{r},\omega))+\left(\frac{i\omega}{c}-\mu_a(\mathbf{r})\right)G(\mathbf{r},\omega)=-\delta(\mathbf{r}_d,\omega). \tag{5}$$

The equations are solved numerically utilizing a finite difference method. The tumor location and geometry are used to segment the inverse problem into two regions, tumor and background, over which the volume integrals in Eq. (3) are computed. Equation (4) is then solved for the absorption perturbations $\Delta\mu_a o$ (background) and $\Delta\mu_a t$ (tumor) and for the diffusion perturbations ΔDo (background) and ΔDt (tumor). The diffusion perturbations are easily transformed into scattering perturbations using the following equation:

$$\Delta\mu_s'=\mu_s'^{(i-1)}\left(\frac{1}{1+3\mu_s'^{(i-1)}\Delta D}-1\right). \tag{6}$$

Two assumptions were necessary to attempt the segmentation. First the different tumor information from the ultrasound images were averaged together to give a single estimate of the

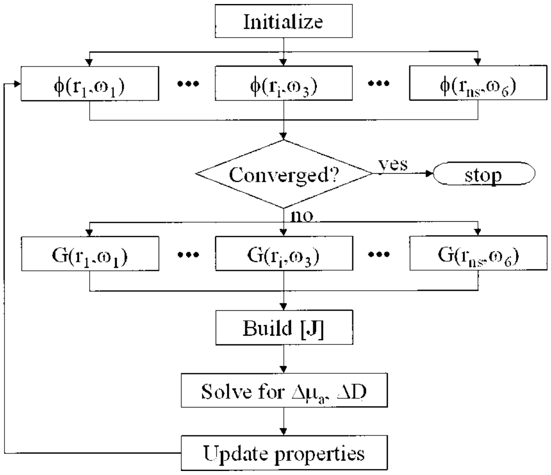

Fig. 5 Flow chart depicting our segmented reconstruction algorithm utilizing parallel processing.

size and location. Second, it was assumed that the tumor was symmetric; this assumption removed any dependence on the relative position of the sources and detectors to the tumor. Additionally, it reduced the number of forward and adjoint problems, five source-detector positions became three independent positions along a given direction, see Figure 2.

The algorithm is depicted in Figure 5. The initial estimates for the optical properties are based on a semi-infinite homogeneous analytic fit. Each box containing Φ or G represents a three-dimensional finite-difference computation for those variables [i.e., a solution to Eq. (1) or (5), respectively]. These computations for each source/detector position and for each frequency are done in parallel. The building of the Jacobian and its solution are done on a single processor. The solution of Eq. (4) is found using simultaneous iterative reconstruction technique (SIRT). The algorithm iterates until convergence is achieved.

The size of the domain was approximated to be $8\ \text{cm} \times 8\ \text{cm} \times 4\ \text{cm}$, with a grid size resolution of 0.125 cm. The number of forward problem solutions for horizontal or vertical simulations was 18 (6 frequencies×3 source positions), equivalent to the number of adjoint problem solutions. These simulations took approximately 3 min/iteration on 19 processors. The number of forward problem solutions for both directions was 36 (6 frequencies×6 source positions), equivalent to the number of adjoint problem solutions. These simulations took 6 min/iteration on 19 processors.

The source strength, an unknown experimental quantity, is removed from the analysis by normalizing the data with a single frequency measurement [i.e., $\Phi^m(\mathbf{r},\omega_i) = \Phi^m(\mathbf{r},\omega_i)/\Phi^m(\mathbf{r},\omega_o)$, where $\omega_o \neq \omega_i$]. A series of numerical tests were conducted on this segmented reconstruction approach using the experimental geometry and we found that six frequencies (including ω_o) were adequate to yield good least-squares fits for a single source-detector pair.

The semi-infinite homogeneous analytic fits are done by iteratively fitting to the semi-infinite analytic solution

$$\Phi(\mathbf{r},\omega) = \frac{S_o}{4\pi D}\left(\frac{e^{ik\mathbf{r}_1}}{\mathbf{r}_1} - \frac{e^{ik\mathbf{r}_2}}{\mathbf{r}_2}\right), \tag{7}$$

Table 2 Normal breast semi-infinite homogeneous analytic fits for μ_a and μ_s' and their χ_v^2 ($\Sigma_{NM}(\Phi_i^m - \Phi_i^c)^2/\sigma_i^2$/DOF) values for amplitude and phase. The direction refers to the measurement sets, i.e., horizontal refers to the source-detector pairs oriented parallel to the sagittal plane (medial-lateral), vertical refers to the source-detector pairs oriented parallel to the axial plane (up-down), both refers to using both horizontal and vertical together.

λ (nm)	Direction	μ_a (cm^{-1})	μ_s' (cm^{-1})	χ_v^2 (amp)	χ_v^2 (phase)
674	Horizontal	0.041	9.6	0.020	0.087
674	Vertical	0.043	9.5	0.015	0.19
674	Both	0.042	9.6	0.019	0.14
782	Horizontal	0.045	8.9	0.16	0.41
782	Vertical	0.044	9.0	0.11	0.57
782	Both	0.045	8.9	0.14	0.49
803	Horizontal	0.035	8.4	0.094	0.38
803	Vertical	0.034	8.5	0.049	1.4
803	Both	0.035	8.5	0.075	0.91
849	Horizontal	0.049	8.2	0.023	0.093
849	Vertical	0.046	8.4	0.025	0.55
849	Both	0.046	8.3	0.025	0.33

where

$$\mathbf{r}_1 = \sqrt{(x-x_s)^2 + (y-y_s)^2 + (z-z_s)^2},$$

$$\mathbf{r}_2 = \sqrt{(x-x_s)^2 + (y-y_s)^2 + (z+z_s+2z_b)^2},$$

$$k = \sqrt{\frac{i\omega}{cD} - \frac{\mu_a}{D}}, \quad (x_s, y_s, z_s)$$

is the source location and z_b is defined as $1/\alpha$. The fitting was done by using a Taylor series expansion of $\Phi(\mathbf{r},\omega)$ with respect to the optical properties, that is,

$$\Phi^m(\mathbf{r},\omega) = \Phi^c(\mathbf{r},\omega) + \frac{\partial\Phi^c(\mathbf{r},\omega)}{\partial\mu_a}\Delta\mu_a + \frac{\partial\Phi^c(\mathbf{r},\omega)}{\partial D}\Delta D + \ldots,$$

where the derivatives are easily determined from Eq. (6). The same six frequencies are used in the segmented reconstruction. Additionally, because we are fitting to a homogeneous solution here, the measurements for the different positions are averaged together as they all share the same source-detector separation and are not supplying additional positional information to the semi-infinite solution.

3 Results and Discussion

3.1 Semi-infinite Analytic

The results from the homogeneous semi-infinite analytic fits for the normal breast are listed in Table 2 and for the breast

Table 3 Breast with lesion semi-infinite homogeneous analytic fits for μ_a and μ_s' and their χ_v^2 values for amplitude and phase, similar to Table 2. These are also the initial conditions for the segmented reconstruction.

λ (nm)	Direction	μ_a (cm^{-1})	μ_s' (cm^{-1})	χ_v^2 (amp)	χ_v^2 (phase)
674	Horizontal	0.061	8.3	0.033	0.19
674	Vertical	0.071	9.8	0.036	0.18
674	Both	0.066	9.0	0.034	0.40
782	Horizontal	0.056	8.0	0.16	0.52
782	Vertical	0.064	9.8	0.086	0.41
782	Both	0.059	8.8	0.12	0.84
803	Horizontal	0.046	7.6	0.094	0.50
803	Vertical	0.066	9.8	0.044	0.20
803	Both	0.056	8.6	0.11	1.5
849	Horizontal	0.061	7.4	0.034	0.19
849	Vertical	0.072	9.7	0.0081	0.059
849	Both	0.065	8.4	0.027	0.93

with the lesion in Table 3. The χ_v^2 values validate the goodness of fit since the values are 1.5 or less. The number of degrees of freedom (DOF) is the number of source-detector pairs $(10 \text{ or } 5) \times$ number of frequencies (74)—the number of parameters (two for semi-infinite and four for segmented reconstruction). Generally, for testing goodness of fit one would want the values to lie between 1.5 and 0.5, when the values are less than 0.5 it is generally believed that the noise was overestimated.

In Figure 6, the homogeneous semi-infinite analytic optical properties for both breasts are plotted versus wavelength. The absorption coefficient shows an *increase* of approximately 48% from the normal breast, consistent with the presence of the tumor. The scattering coefficient exhibits a *decrease* of ~11% for the horizontal measurements and an *increase* of ~11% for the vertical measurements from the normal breast. Using both sets of measurements, the average difference between the breasts is less than 1% for the scattering coefficient. These semi-infinite analytic results provide a simple and fast way of determining the presence of a tumor, however the optical properties are clearly insufficient for further diagnosis of the tumor. Therefore, we have advanced the reconstruction by assuming the presence of a tumor with the geometry provided by the ultrasound images.

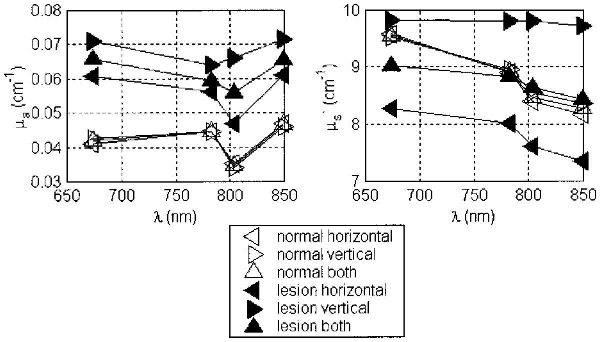

Fig. 6 Semi-infinite homogeneous analytic fits for the optical properties of the normal breast (open triangles, see Table 2) and the breast with lesion (solid triangles, see Table 3).

Table 4 Simulation parameters for the base case and the sensitivity studies. Direction is the set of measurements used for the given simulation, *a* is the *y*-axis length of the tumor, *b* is the *x*-axis length of the tumor, *c* is the *z*-axis length of the tumor, and *zc* is the center of the tumor below the skin surface. $n_{\text{in}}/n_{\text{out}}$ is the index mismatch between the tissue (n_{in}) and the air (n_{out}). The base case is the optimal choice of the listed parameters. The sensitivity studies focus on directional sensitivity of the measurements (horizontal and vertical), size of the tumor (bigger and smaller), and the index mismatch of the tissue–air interface (greater and less).

Experiment	Direction	*a*	*b*	*c*	*zc*	$n_{\text{in}}/n_{\text{out}}$
Base	Both	2.13	1.68	1.135	1.1975	1.36
Horizontal	Horizontal	2.13	1.68	1.135	1.1975	1.36
Vertical	Vertical	2.13	1.68	1.135	1.1975	1.36
Bigger	Both	2.343	1.848	1.2485	1.1975	1.36
Smaller	Both	1.917	1.512	1.0215	1.1975	1.36
Greater	Both	2.13	1.68	1.135	1.1975	1.40
Less	Both	2.13	1.68	1.135	1.1975	1.333

3.2 Segmented Reconstruction

The segmented reconstruction parameters are listed in Table 4 along with the parameters for a series of sensitivity studies. The optimal estimate of all the parameters is the base case. The results of the segmented reconstruction fit for the base case are listed in Table 5. For all four wavelengths, the tumor properties had *increased* absorption, on average 3.4× the background, and *decreased* scattering, on average 0.41× the background. The $\chi_v^{(2)}$ are again very good, in fact the segmented reconstruction values are improved compared to those

Table 5 Base case results from the segmented reconstruction and their χ_v^2 values for amplitude and phase ($\mu_a o, \mu_s' o$ are background and $\mu_a t, \mu_s' t$ are tumor values). The base case represents the optimal choice for the simulation parameters listed in Table 4.

λ (nm)	$\mu_a o$ (cm^{-1})	$\mu_s' o$ (cm^{-1})	$\mu_a t$ (cm^{-1})	$\mu_s' t$ (cm^{-1})	χ_v^2 (amp)	χ_v^2 (phase)
674	0.057	9.5	0.17	4.1	0.032	0.29
782	0.050	9.4	0.18	3.6	0.12	0.68
803	0.047	9.0	0.15	4.2	0.16	1.1
849	0.054	8.9	0.21	3.3	0.020	0.64

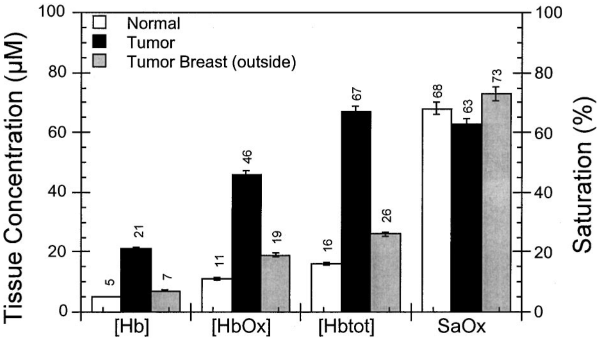

Fig. 7 Physiological parameters calculated from wavelength-dependent absorption: Tissue deoxyhemoglobin [Hb], oxyhemoglobin [HbOx], and total [$\mathrm{Hb}_{\mathrm{tot}}$] concentration ($\mu$M); Hemoglobin oxygen saturation (%SOx). Values determined for normal breast, tumor, and tumor-containing breast outside of tumor region.

recovered using the homogeneous semi-infinite model (using both measurement directions) further validating our segmented model.

The background absorption coefficients from the segmented reconstruction are generally similar to the absorption coefficients determined for the breast lesion using the semi-infinite homogeneous model. The segmented background scattering coefficients are also close to the semi-infinite scattering properties.

Overall, the optical properties of the tumor show dramatic contrast with both normal tissue and tumor-breast background. The *increase* in μ_a is due to hemoglobin absorption; the principal NIR-absorbing component of highly vascular tumors. Previous *in vivo* studies suggest that tumors can display two to fivefold higher blood volume fractions than uninvolved breast tissue.[49–51] Our segmentation scheme reveals substantially higher tumor/background contrast than observed using a homogeneous semi-infinite analytical model that averages properties over a large volume. In addition, the reduced scattering (μ_s') values in the tumor were, on average, about half those of normal tissue. This feature suggests the core of the tumor has a low cellular and/or extracellular matrix density. Interestingly, since fluid content also provides contrast for ultrasound images, combining optical and ultrasound observations indicates the tumor core is likely to be a necrotic, blood-filled region dominated by particles that have low scattering cross sections and/or low density (compared to normal, well-differentiated breast tissue). This view coincides well with histopathology data showing the tumor to be poorly differentiated and malignant.

Further diagnostic insight is provided by calculating the physiological properties of normal breast, tumor, and tumor breast outside the tumor region. Assuming the principal absorbers are oxy- and deoxyhemoglobin (HbOx and Hb, respectively), least squares fits of calculated μ_a values (from Tables 2 and 5 for normal and tumor breast, respectively) to molecular extinction coefficients for each component at the four measured wavelengths[1] can be used to determine [HbOx], [Hb], and percentage hemoglobin saturation ($\mathrm{SOx} = 100\times[\mathrm{HbOx}]/[\mathrm{Hb}_{\mathrm{tot}}]$; and $[\mathrm{Hb}_{\mathrm{tot}}]=[\mathrm{Hb}]+[\mathrm{HbOx}]$).

These results, summarized in Figure 7, show clear differences between tumor and normal tissue. Most dramatic is the approximately fourfold *increase* in total hemoglobin content at the tumor (67 μM) vs normal tissue (16 μM). Hemoglobin contrast is reduced to a factor of 2.6 when the tumor site and surrounding tumor-containing breast tissue (25.5 μM) are compared. SOx values are lower at the tumor site (63%) vs normal (68%) and surrounding tumor-containing breast (73%). Differences are likely due to the oxygen extraction demands of rapidly proliferating, metabolically active tumor cells. The reduced saturation value at the tumor is consistent with the measured elevation in tumor hemoglobin, since both blood and oxygen are required to sustain tumor growth. Others have measured similar elevated tumor hemoglobin concentration and low SOx values noninvasively with photon migration techniques.[48,49] Interestingly, both total hemoglobin and SOx values are slightly elevated in the tumor-containing surrounding breast versus the contra-lateral normal side. This suggests that physiological changes occur beyond the ultrasound-designated tumor margin that are detectable with light. For example, a high blood flow, well-vascularized region could extend beyond the ultrasound-defined tumor dimension. This observation is consistent with the notion of a hypoxic, necrotic tumor core surrounded by a well-vascularized, normoxic cortex that provides the leading edge for growth.

3.3 Sensitivity Studies

Table 4 lists the parameters for a series of sensitivity studies. We examined the sensitivity of the optical properties to measurement direction, tumor size, and boundary condition. Measurement direction had two options: horizontal (along the axial plane) or vertical (along the sagittal plane). Tumor size was enlarged by 10% along each major axis or was decreased by 10% along each major axis. The boundary condition was either based on an index mismatch of 1.333 or 1.40.

3.3.1 *Measurement direction*

These results tested the sensitivity of the calculated optical properties to the direction that the measurements were taken. Figure 8(a) lists optical property and χ_ν^2 values for the four parameter fits. Some of the χ_ν^2 values are increased relative to the semi-infinite fit. This is caused by the symmetry assumption and is minimized when using both measurement sets together. The tumor absorption was on average 4.1× the background for the horizontal and 2.3× the background for the vertical. The tumor scattering for the horizontal was on average 0.3× the background and 0.55× for the vertical. The base case values lie directly in-between these values illustrating the impact of minimizing the error between the two directions.

The sensitivity can best be depicted by a bar graph showing the average percentage change from the base case for each of the four parameters, see Figure 8(b). The background properties *decreased* from the base case for the horizontal measurements ~10% and *increased* for the vertical ~15%. The tumor properties showed more sensitivity to the vertical direction, especially the scattering (~45%). Finally, the base case optical properties were more similar to the horizontal optical properties, indicating that the base case segmented reconstruction fits were more sensitive to the horizontal measurements than the vertical. This is consistent with the vertical measure-

λ(nm)	Direction	$\mu_a o$(cm^{-1})	$\mu_s' o$(cm^{-1})	$\mu_a t$(cm^{-1})	$\mu_s' t$(cm^{-1})	χ_ν^2(amp)	χ_ν^2(phase)
674	Horizontal	0.053	8.8	0.20	2.3	0.030	0.19
674	Vertical	0.066	10.	0.14	5.3	0.035	0.16
782	Horizontal	0.049	8.4	0.17	3.1	0.17	0.55
782	Vertical	0.056	10.	0.14	5.3	0.089	0.37
803	Horizontal	0.036	8.0	0.18	2.8	0.079	0.53
803	Vertical	0.061	10.	0.11	7.0	0.073	0.13
849	Horizontal	0.052	7.9	0.22	1.7	0.041	0.23
849	Vertical	0.062	10.	0.17	5.0	0.0085	0.025

(a)

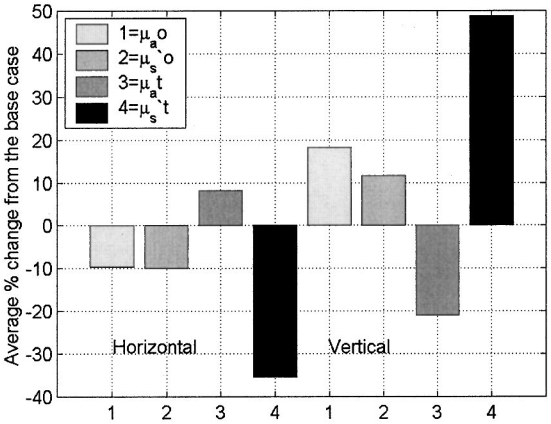

(b)

Fig. 8 (a) Directional sensitivity segmented reconstruction results and their χ_ν^2 values for amplitude and phase. Horizontal uses just the horizontal measurement set and vertical uses just the vertical measurement set, see Figure 2 for orientation and Table 4 for parameters. (b) Average percentage change of the segmented reconstruction optical properties over the four optical wavelengths from the base case to the horizontal measurement set simulation (left four bars) and the vertical measurement set simulation (right four bars). The horizontal measurement set simulations show less change from the base case than the vertical set measurement simulations. This is consistent with the horizontal measurement set being less sensitive to the symmetry assumption of the tumor than the vertical measurement set.

λ(nm)	Size	$\mu_a o$(cm^{-1})	$\mu_s' o$(cm^{-1})	$\mu_a t$(cm^{-1})	$\mu_s' t$(cm^{-1})	χ_ν^2(amp)	χ_ν^2(phase)
674	Bigger	0.058	9.7	0.15	4.4	0.032	0.28
674	Smaller	0.058	9.4	0.19	3.8	0.032	0.31
782	Bigger	0.049	9.5	0.15	4.2	0.12	0.67
782	Smaller	0.051	9.3	0.21	3.2	0.12	0.70
803	Bigger	0.046	9.1	0.13	4.7	0.16	1.0
803	Smaller	0.048	8.9	0.17	4.1	0.15	1.1
849	Bigger	0.053	9.0	0.18	3.8	0.020	0.60
849	Smaller	0.056	8.8	0.23	3.2	0.057	0.98

(a)

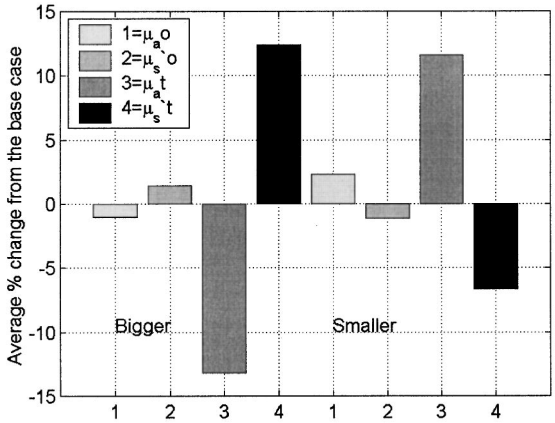

(b)

Fig. 9 (a) Tumor size sensitivity segmented reconstruction results. Bigger refers to an increase in tumor size and smaller refers to a decrease in tumor size, see Table 4 for parameters. (b) Average percentage change of the segmented reconstruction optical properties over the four optical wavelengths from the base case to the bigger tumor size simulation (left four bars) and the smaller tumor size simulation (right four bars). The tumor optical properties had the most sensitivity, specifically its absorption coefficient. As the tumor increased its absorption decreased and its scattering increased, when the tumor decreased the opposite occurred. Additionally, the χ_ν^2 values for the bigger tumor size were slightly less than the base case values. This implies that the tumor was optically larger than the ultrasound size.

ments being more sensitive to the symmetry assumption for the tumor geometry. This is clear since the vertical measurement set is aligned with the major axis of the ellipse. Therefore the vertical measurement set will be more sensitive to the tumor optical properties than the horizontal measurement set.

3.2.2 *Tumor size*

This study observed the impact of changing the size of the tumor on the optical properties. Figure 9(a) lists the results from the segmented reconstruction fit. The χ_ν^2 values are smaller than the base case for the larger tumor, implying that the optical tumor margins might in fact be larger than was estimated from the ultrasound. The tumor absorption was about 3.0× the background for the larger size and about 3.75× for the smaller size. The tumor scattering was about 0.46× the background for the larger size and about 0.39× for the smaller size.

Figure 9(b) shows the average over the wavelengths for the percentage change from the base case for the tumor size sensitivity. Overall, the size sensitivity is quite reduced from the directional sensitivity. The background properties did not change significantly from the base case. However, the tumor properties showed greater sensitivity; particularly the absorption increasing or decreasing when size decreased and increased, respectively. The volume change ($\Delta V = V' - V$, where V' is the new volume and V is the base case volume) of the tumor is directly related to the change in $\Delta\mu_a$ ($\mu_a t - \mu_a o$) as follows: $\Delta\mu_a' = \Delta\mu_a/(1+\Delta V/2V)$. $\Delta\mu_s'$ also changed with volume; increasing when the volume increased ~6% and decreasing when the volume decreased ~3%, however there was no clear functional relationship between the two parameters.

3.2.3 *Index mismatch*

This last study focused on changing the index mismatch at the tissue–air interface, essentially testing the importance of the boundary condition assumption. Figure 10(a) lists the results from the segmented reconstruction fit. The χ_ν^2 values are very similar for all cases of the index mismatch parameter, including the base case. The tumor absorption was on average 3.4× the background for both mismatch indices. The tumor scatter-

λ(nm)	n_{in}/n_{out}	μ_ao(cm^{-1})	μ_s'o(cm^{-1})	μ_at(cm^{-1})	μ_s't(cm^{-1})	χ_v^2(amp)	χ_v^2(phase)
674	1.4	0.058	9.4	0.17	4.0	0.031	0.29
674	1.333	0.057	9.5	0.17	4.1	0.032	0.29
782	1.4	0.050	9.3	0.18	3.5	0.12	0.69
782	1.333	0.050	9.4	0.18	3.6	0.12	0.68
803	1.4	0.047	9.0	0.15	4.2	0.15	1.1
803	1.333	0.047	9.0	0.15	4.3	0.16	1.1
849	1.4	0.054	8.9	0.21	3.3	0.019	0.64
849	1.333	0.054	8.9	0.21	3.4	0.021	0.64

(a)

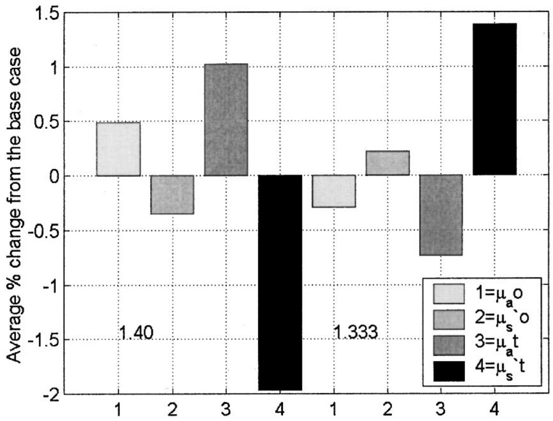

(b)

Fig. 10 (a) Index mismatch sensitivity segmented reconstruction results. 1.4 refers to the index mismatch at the tissue–air interface to be 1.4 and 1.333 refers to the index mismatch at the tissue–air interface to be 1.333. (b) Average percentage change of the segmented reconstruction optical properties over the four optical wavelengths from the base case to the 1.40 tissue–air interface index mismatch simulation (left four bars) and the 1.333 tissue–air interface index mismatch simulation (right four bars). Overall the index mismatch did not impact our results, suggesting that the optical properties are not very sensitive to this parameter. Additionally, the χ_v^2 values were similar for all cases of the index mismatch parameter supporting the finding that this parameter did not affect our results.

ing was on average 0.4× the background for both mismatch indices. These factors are very similar to the base case factors.

Figure 10(b) shows the average percentage change from the base case for the index mismatch simulations (over the four wavelengths). The sensitivity of the optical properties was very small and all the properties were affected ~1.5% or less. This indicates that this assumption did not affect our solution.

4 Conclusions

Semi-infinite homogeneous analytic fits are very useful for providing a gross determination of tumor optical properties. However, significant physiological information in tumors and surrounding tissues may be lost in this averaging procedure. Our use of ultrasound localization with diffuse optical mammography provides improved optical information about the tumor and background tissue. From this reconstruction, a sharp contrast in the optical properties was readily determined. A three to fourfold *increase* in the absorption coefficient and nearly 50% reduction in scattering coefficient, relative to background, were found. These values are consistent with expected properties of a highly vascularized tumor with a blood-filled, necrotic core. Physiological property calculations confirm this view, revealing fourfold greater tumor hemoglobin concentration than normal breast (67 vs 16 μM) and low tumor SOx values of 63% (vs 73% and 68% in the region surrounding the tumor and the opposite normal tissue, respectively). Comparison of the semi-infinite results from the normal breast to the background properties of the lesion-containing breast yields further information about tissues surrounding the tumor. They suggest that alterations in vascular density and tissue inflammatory response occur beyond the ultrasound-defined tumor margins.

A series of sensitivity studies were conducted to ascertain the relative importance of some of our basic assumptions. A test of measurement direction revealed that the assumption of tumor symmetry in shape and orientation was quite sensitive, but its impact was minimized when using both horizontal and vertical measurement sets together. In a test of the tumor size estimate, an increase in tumor size resulted in better model fits. This suggests that the tumor may be larger when defined by light than by ultrasound.

Although our analysis is reported only for a single subject, frequency domain-DOT images obtained from this hand-held probe reveal new tumor diagnostic criteria and substantially enhanced contrast in both absorption and scattering. The *increase* in measured absorption and *decrease* in scattering at the tumor versus surrounding tissue further underscores a key practical benefit to our quantitative approach. Ultimately, the combination of hand-held ultrasound and optical probes may allow rapid, functional characterization of subcutaneous inhomogeneities. We expect this information will be particularly useful in screening pre- and perimenopausal women with radiographically dense breast tissue, where distinguishing between malignant and benign lesions and understanding effects of therapies and disease progression can be highly problematic.

Acknowledgments

We gratefully acknowledge Pavlos Protopapas, who helped convert our software to parallel. This work was made possible, in part, through access to the Laser Microbeam and Medical Program (LAMMP) and the Chao Family Cancer Center at the University of California, Irvine. These facilities are supported by the National Institutes of Health (NCRR and NCI) under Grant Nos. RR-01192 and CA-62203, respectively. Support was also provided by the NIH Institute of General Medical Sciences (GM-50958), the Department of Energy (DOE No. DE-FG03-91ER61227), the U.S. Army Breast Cancer Research Program, and the Beckman Foundation. A.G.Y. gratefully acknowledges partial support from the NIH (No. CA75124-01) and the U.S. Army (DAMD17-97-1-7272).

References

1. J. B. Fishkin et al., ''Frequency-domain photon migration measurements of normal and malignant tissue optical properties in a human subject,'' *Appl. Opt.* **36**, 10–20 (1997).
2. S. Fantini et al., ''Assessment of the size, position, and optical properties of breast tumors in vivo by noninvasive optical methods,'' *Appl. Opt.* **37**, 1982–1989 (1998).
3. D. Grosenick et al., ''Development of a time-domain optical mam-

mograph and first in vivo applications,'' *Appl. Opt.* **38**, 2927–2943 (1999).
4. G. Müller, J. Beuthan, and O. Minet, ''Laser-generated Diffusion Tomograms in the Near Infrared,'' *Laser Phys.* **6**, 589–595 (1996).
5. S. A. Walker et al., ''Image reconstruction by backprojection from frequency-domain optical measurements in highly scattering media,'' *Appl. Opt.* **36**, 170–179 (1997).
6. S. B. Colak et al., ''Tomographic image reconstruction from optical properties in light-diffusing media,'' *Appl. Opt.* **36**, 180–213 (1997).
7. O. Dorn, ''A transport-backtransport method for optical tomography,'' *Inverse Probl.* **14**, 1107–1130 (1998).
8. J. C. Schotland, ''Continuous-wave diffusion imaging,'' *J. Opt. Soc. Am. A* **14**, 275–279 (1997).
9. C. L. Matson et al., ''Three-dimensional tumor localization in thick tissue with the use of diffuse photon-density waves,'' *Appl. Opt.* **36**, 214–220 (1997).
10. X. D. Li et al., ''Diffraction tomography for biochemical imaging with diffuse-photon density waves,'' *Opt. Lett.* **22**, 573–575 (1997).
11. X. Cheng and D. A. Boas, ''Diffuse optical reflection tomography with continuous-wave illumination,'' *Opt. Express* **3**, 118–123 (1998).
12. D. N. Pattanayak and A. G. Yodh, ''Diffuse optical 3D-slice imaging of bounded turbid media using a new integro-differential equation,'' *Opt. Express* **4**, 231–240 (1999).
13. C. L. Matson and H. Li, ''Analysis of the forward problem with diffuse photon density waves in turbid media by use of a diffraction tomography model,'' *J. Opt. Soc. Am. A* **16**, 455–466 (1999).
14. T. Durduran et al., ''Algorithms for 3D localization and imaging using near-field diffraction tomography with diffuse light,'' *Opt. Express* **4**, 247–262 (1999).
15. J. C. Schotland et al., ''Photon hitting density,'' *Appl. Opt.* **32**, 448–453 (1993).
16. S. R. Arridge, ''Photon-measurement density functions. Part 1: Analytic forms,'' *Appl. Opt.* **34**, 7395–7409 (1995).
17. S. R. Arridge and M. Schweiger, ''Photon-measurement density functions. Part 2: Finite-element-method calculations,'' *Appl. Opt.* **34**, 8026–8037 (1995).
18. M. A. O'Leary et al., ''Experimental images of heterogeneous turbid media by frequency-domain diffusing-photon tomography,'' *Opt. Lett.* **20**, 426–428 (1995).
19. K. D. Paulsen and H. Jiang, ''Spatially varying optical property reconstruction using a finite element diffusion equation approximation,'' *Med. Phys.* **22**, 691–701 (1995).
20. H. Jiang et al., ''Simultaneous reconstruction of optical absorption and scattering maps in turbid media from near-infrared frequency-domain data,'' *Opt. Lett.* **20**, 2128–2130 (1995).
21. H. Jiang, K. D. Paulsen, and U. L. Österberg, ''Optical image reconstruction using DC data: simulations and experiments,'' *Phys. Med. Biol.* **41**, 1483–1498 (1996).
22. W. Cai et al., ''Time-resolved optical diffusion tomographic image reconstruction in highly scattering media,'' *Proc. Natl. Acad. Sci. USA* **93**, 13561–13564 (1996).
23. A. H. Hielscher, ''Model-Based Iterative Image Reconstruction for Photon Migration Tomography,'' in *Computational, Experimental and Numerical Methods for Solving Ill-posed Inverse Imaging Problems: Medical and Nonmedical Applications*, *Proc. SPIE* **3171**, 106–117 (1997).
24. J. Chang et al., ''Optical imaging of anatomical maps derived from magnetic resonance images using time-independent optical sources,'' *IEEE Trans. Med. Imaging* **16**, 68–77 (1997).
25. D. Y. Paithankar et al., ''Imaging of fluorescent yield and lifetime from multiply scattered light reemitted from random media,'' *Appl. Opt.* **36**, 2260–2272 (1997).
26. E. M. Sevick-Muraca et al., ''Role of higher-order scattering in solutions to the forward and inverse optical-imaging problems in random media,'' *Appl. Opt.* **36**, 9058–9067 (1997).
27. Y. Yao et al., ''A Born Type Iterative Method for Imaging of Heterogeneous Scattering Media and its Application to Simulated Breast Tissue,'' in *Optical Tomography and Spectroscopy of Tissue: Theory, Instrumentation, Model and Human Studies II*, *Proc. SPIE* **2979**, 232–240 (1997).
28. Y. Yao et al., ''Frequency-domain optical imaging of absorption and scattering distributions by a Born iterative method,'' *J. Opt. Soc. Am. A* **14**, 325–342 (1997).
29. R. Model et al., ''Reconstruction algorithm for near-infrared imaging in turbid media by means of time-domain data,'' *J. Opt. Soc. Am. A* **14**, 313–324 (1997).
30. F. Gao et al., ''The forward and inverse models in time-resolved optical tomography imaging and their finite-element method solutions,'' *Image Vis. Comput.* **16**, 703–712 (1998).
31. M. V. Klibanov et al., ''A fast and accurate imaging algorithm in optical/diffusion tomography,'' *Inverse Probl.* **13**, 1341–1361 (1997).
32. M. V. Klibanov and T. R. Lucas, ''Numerical solution of a parabolic inverse problem in optical tomography using experimental data,'' *SIAM (Soc. Ind. Appl. Math.) J. Appl. Math.* **59**, 1763–1789 (1999).
33. Y. A. Gryazin et al., ''Imaging the diffusion coefficient in a parabolic inverse problem in optical tomography,'' *Inverse Probl.* **15**, 373–397 (1999).
34. M. F. Maritz et al., ''Recovery of the absorption coefficient from diffused reflected light using a discrete diffusive model,'' *SIAM (Soc. Ind. Appl. Math.) J. Appl. Math.* **59**, 58–71 (1998).
35. T. H. Pham, O. Coquoz, J. B. Fishkin, E. Anderson, and B. J. Tromberg, ''Broad-bandwidth frequency-domain instrument for quantitative tissue optical spectroscopy,'' *Rev. Sci. Instrum.* **71**, 1–14 (2000).
36. Q. Zhu, T. Durduran, V. Ntziachristos, M. Holboke, and A. G. Yodh, ''Imager that combines near-infrared diffusive light and ultrasound,'' *Opt. Lett.* **24**, 1050–1052 (1999).
37. A. G. Yodh and B. Chance, ''Spectroscopy and Imaging with Diffusing Light,'' *Phys. Today* **48**, 34–40 (1995).
38. R. A. J. Groenhuis et al., ''Scattering and absorption of turbid materials determined from reflection measurements,'' *Appl. Opt.* **22**, 2456 (1983).
39. S. R. Arridge, ''Optical tomography in medical imaging,'' *Inverse Probl.* **15**, R41–R93 (1999).
40. W. Zhu et al., ''Wavelet-Based Multiresolution Regularized Least Squares Reconstruction Approach for Optical Tomography,'' *IEEE Trans. Med. Imaging* **16**, 210–217 (1997).
41. S. R. Arridge and M. Schweiger, ''A gradient-based optimisation scheme for optical tomography,'' *Opt. Express* **2**, 213–226 (1998).
42. M. J. Eppstein et al., ''Biomedical optical tomography using dynamic parameterization and Bayesian conditioning on photon migration measurements,'' *Appl. Opt.* **38**, 2138–2150 (1999).
43. J. C. Ye et al., ''Modified distorted Born iterative method with an approximate Frechet derivative for optical diffusion tomography,'' *J. Opt. Soc. Am. A* **16**, 1814–1826 (1999).
44. J. C. Ye et al., ''Optical diffusion tomography by iterative-coordinate-descent optimization in a Bayesian framework,'' *J. Opt. Soc. Am. A* **16**, 2400–2412 (1999).
45. K. D. Paulsen and H. Jiang, ''Enhanced frequency-domain optical image reconstruction in tissues through total-variation minimization,'' *Appl. Opt.* **35**, 3447–3458 (1996).
46. H. Jiang et al., ''Frequency-domain optical image reconstruction in turbid media: an experimental study of single-target detectability,'' *Appl. Opt.* **36**, 52–63 (1997).
47. H. Jiang et al., ''Improved continuous light diffusion imaging in single- and multi-target tissue-like phantoms,'' *Phys. Med. Biol.* **43**, 675–693 (1998).
48. B. W. Pogue et al., ''Spatially variant regularization improves diffuse optical tomography,'' *Appl. Opt.* **38**, 2950–2961 (1999).
49. S. Fantini, S. A. Walker, M. A. Franceschini, K. T. Moesta, P. M. Schlag, M. Kaschke, and E. Gratton, ''Assessment of the size, position, and optical properties of breast tumors in vivo by non-invasive optical methods,'' *Appl. Opt.* **37**, 1982–1989 (1998).
50. T. O. McBride, B. Pogue, E. D. Gerety, S. B. Poplack, U. L. Osterberg, and K. D. Paulsen, ''Spectroscopic diffuse optical tomography for the quantitative assessment of hemoglobin concentration and oxygen saturation in breast tissue,'' *Appl. Opt.* **38**(25), 5480–5491 (1999).
51. B. J. Tromberg, N. Shah, R. Lanning, A. Cerussi, J. Espinoza, T. Pham, L. Svaasand, and J. Butler, ''Noninvasive *in vivo* characterization of breast tumors using photon migration spectroscopy,'' *Neoplasia* **2**(1-2), 26–40 (2000).